

Quantum Optimal Control for Atomic Fountain Interferometry

Michael H. Goerz^a, Mark A. Kasevich^b, and Vladimir S. Malinovsky^a

^aU.S. Army Research Laboratory, Computational and Information Sciences Directorate,
Adelphi, MD 20783, USA.

^bDepartment of Physics, Stanford University, Stanford, CA 94305, USA.

ABSTRACT

We present an analysis of the robustness of existing analytic schemes for the implementation of an atomic fountain interferometer, and develop concepts for improving this robustness through the use of optimal control theory. For an interferometer operating in the Raman regime, we consider an implementation that manipulates the atomic momentum states with a series of Rabi pulses, and analyze how robust the population dynamics are with respect to variations in the effective pulse amplitude seen by the atoms in the atomic clouds, and variations in the initial velocity of the atoms relative to the rest frame. We then show that using rapid adiabatic passage to implement momentum transfer can significantly improve this robustness. Finally, we formulate the most general control conditions for an atomic fountain interferometer and design a functional that can be used for an ensemble optimization over the robustness landscape. We show preliminary results of optimizing the system using Krotov’s method, suggesting that optimal control may be able to significantly enhance the robustness of atom interferometers.

Keywords: quantum sensing, atom interferometry, optimal control

1. INTRODUCTION

Atom interferometry is a technology of unrivaled precision to measure acceleration and gravitational gradients.¹ Conceptually, atom interferometers operate identically to standard light interferometers: A “beam” is split into two spatially separate pathways. As they propagate, a difference in path length or other external influences induces a relative phase between the two pathways. The beams are then subjected to a “mirror” and a final “beamsplitter” to recombine them, resulting in an interference pattern depending on the accumulated relative phase. In an atom interferometer, the “beams” consist of atomic matter waves instead of electromagnetic waves. Since atoms, unlike photons, have a non-zero rest mass, such an interferometer is sensitive to accelerations and gravitational fields. This opens up many applications. Atom interferometry may be used in fundamental physics for testing the mass equivalence principle or detecting gravitational waves. For more applied usage, it enables gravitational sensing with unprecedented precision, and inertial navigation.

However, unlike for light, there are no immediate mirrors or beamsplitters for atomic matter waves. Instead, the atoms must be manipulated with light-matter interaction.^{2,3} We consider here the specific implementation of an atomic fountain interferometer. There, a cloud of Rubidium atoms is launched into a ten-meter tower. Immediately after the launch, two counter-propagating standing laser waves drive a two-photon Raman transition, imparting the photon momentum as discrete momentum kicks to the atoms. With proper pulse shaping, the atomic cloud is split into a quantum superposition of two momentum states, separating the wave packet as it travels up the tower. At the turning point, another shaped laser pulse acts as the “mirror”, reversing the momentum space splitting. Finally, as the cloud reaches the bottom of the tower, where a final laser pulse recombines the wave packet such that a relative phase between the two components of the wave packet results in interference fringes in the two ports of the output detector.

The shaped laser pulses implementing the effective “beamsplitter” and “mirror” for matter waves are a prime example of *quantum control*, that is, the active manipulation of a quantum system to steer them towards a particular behavior.⁴ Such quantum control is the cornerstone of a “second quantum revolution”⁵ that includes

quantum sensing applications⁶ such as the atom interferometer we are considering here, as well as other technology such as quantum computing.⁷ While there is some room for analytical solutions to quantum control problems, its full potential can only be unlocked with *numerical methods of optimal control* such as GRAPE⁸ or the application of Krotov’s method^{9,10} to quantum control.^{11–16}

Here, we explore the potential for using numerical optimal control theory to ensure robustness of the interferometer: the signal contrast of the interferometer is fundamentally limited by the fact that some atoms in the atomic cloud deviate from the ideal conditions for which the control shapes have been designed: they may experience a reduced pulse amplitude due to the finite transversal width of the laser field relative to the atomic cloud, or they may have a non-zero initial velocity relative to the ideal rest-frame. Using optimal control theory, we may find control fields that are less sensitive to such variations than the best analytically designed schemes; a method that has previously been demonstrated to improve that robustness of implementing entangling gates on trapped Rydberg atoms.¹⁷

By enhancing the signal contrast of the atomic fountain interferometer, we ultimately hope to implement a *robust* interferometer with large momentum space separation, approaching or surpassing previously reached separations of $100\hbar k$.¹⁸ Furthermore, we could miniaturize the current ten-meter tower design while preserving measurement precision, enabling the next generation use of the technology in the field, for gravimetric sensing and inertial navigation.

The paper is structured as follows: In Section 2, we derive a model for the momentum space dynamics of a Rubidium atom interacting with two counter-propagating standing waves. These off-resonantly drive an internal electronic transition of the atom, which effectively results in a two-photon transitions between the levels of a discrete momentum space ladder. In Section 3, we analyze two analytic pulse schemes for implementing a full atomic interferometer: first by a train of Rabi pulses, and second by realizing momentum space transfer via rapid adiabatic passage (RAP). We analyze the robustness of these schemes with respect to variations of the pulse amplitude from the “ideal” value and for non-zero initial velocity of the atoms relative to the rest frame, demonstrating the inherent robustness of the RAP process. In order to explore the possible use of optimal control theory for generating robust control schemes, we formulate the most general control conditions for all parts of the interferometer in Section 4, finding that interference fringes can be robust against relative phases introduced by a non-ideal pulse amplitudes or non-zero initial velocity. In Section 5, we formulate a new functional based on this insight that targets general population transfer, and extend it for an *ensemble optimization*, where the optimization aims to find a single control field that performs well for an average of different effective amplitudes and initial velocities. In Section 6, we show some preliminary results of control fields obtained with this method. Section 7 concludes.

2. MODEL

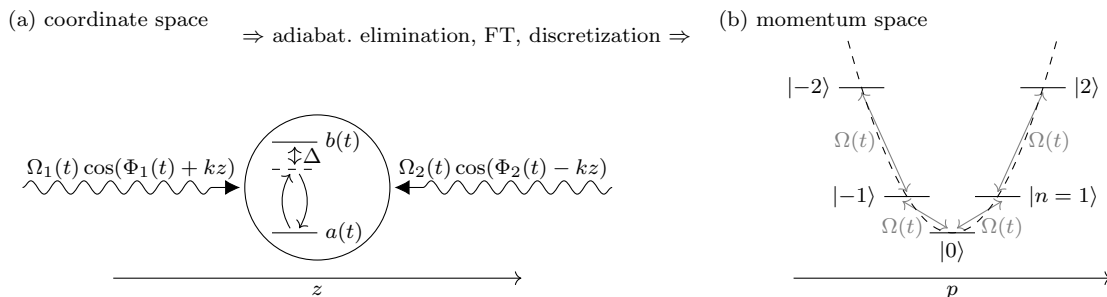


Figure 1. Single atom inside an atomic fountain interferometer. (a) In coordinate space. Two counter-propagating standing wave off-resonantly drive an internal electronic transition of the atom. (b) In momentum space. Performing adiabatic elimination of the excited state, taking the Fourier transform, and discretizing the momentum space leads to a quadratic ladder of momentum states $|n\rangle$ corresponding to momentum $2n\hbar k$, driven by an effective field $\Omega(t)$.

We consider a Rubidium atom having been launched with initial velocity v_0 along the z -axis of an atomic fountain interferometer, evolving under the influence of two counter-propagating laser fields with wavenumber k , and envelopes $\Omega_1(t)$, $\Omega_2(t)$ and time-dependent phases

$$\Phi_1(t) = \omega_0 t + \phi_1(t), \quad \Phi_2(t) = \delta_0 t + \omega_0 t + \phi_2(t), \quad (1)$$

where ω_0 is a common reference frequency, $\phi_1(t)$ and $\phi_2(t)$ are the time-dependent phases relative to this reference, and δ_0 is a static phase offset between the two standing waves. As depicted in Fig. 1 (a), the laser fields off-resonantly drive the atom's D₂ transition $5^2S_{1/2} \rightarrow 5^2P_{2/2}$ ¹⁹ with detuning Δ . For the complex amplitude $a(t)$ of the ground state, the Schrödinger equation coupling to the complex amplitude $b(t)$ of the excited state reads

$$i\hbar \frac{\partial}{\partial t} a(z, t) = -(\hbar\Omega_1(t) \cos(kz + \Phi_1(t)) + \hbar\Omega_2(t) \cos(kz - \Phi_2(t))) b(z, t) + \frac{p^2 a(z, t)}{2m}. \quad (2)$$

For a large detuning Δ , we can adiabatically eliminate the excited state amplitude $b(z, t)$, resulting in

$$i\hbar \frac{\partial}{\partial t} a(z, t) = \left(-\hbar\Omega(t) e^{i\phi(t)} e^{2ikz} - \hbar\Omega(t) e^{-i\phi(t)} e^{-2ikz} - \hbar\Omega_\Delta(t) + \frac{p^2}{2m} \right) a(z, t), \quad (3)$$

with the common light shift

$$\Omega_\Delta(t) = \frac{\Omega_1^2(t)}{4\Delta} + \frac{\Omega_2^2(t)}{4\Delta}, \quad (4)$$

the effective envelope

$$\Omega(t) = \frac{\Omega_1(t)\Omega_2(t)}{4\Delta}, \quad (5)$$

and the effective phase

$$\phi(t) = \phi_1(t) - \phi_2(t) - \delta_0 t. \quad (6)$$

We now transform this into momentum space by taking the Fourier transform to find

$$i\hbar \frac{\partial}{\partial t} a(p, t) = -\hbar\Omega(t) a(-2\hbar k + p, t) e^{i\phi(t)} - \hbar\Omega(t) a(2\hbar k + p, t) e^{-i\phi(t)} + \left(\frac{p^2}{2m} - \hbar\Omega_\Delta(t) \right) a(p, t) \quad (7)$$

Since the state with momentum p couples directly only to the states with momentum $p \pm 2\hbar k$, for a particle moving with velocity v_0 relative to the rest frame, we can make the ansatz

$$a(p, t) = a_n(t) e^{in\phi(t)} \delta(-2\hbar kn + p - mv_0). \quad (8)$$

That is, we introduce a discrete momentum state basis $|n\rangle$ with $n \in \mathbb{Z}$, corresponding to momentum $2n\hbar k$, and find for the probability amplitude $a_n(t)$

$$i\hbar \frac{\partial}{\partial t} a_n(t) = -\hbar\Omega(t) a_{n-1}(t) - \hbar\Omega(t) a_{n+1}(t) + E_n(t) a_n(t) \quad (9)$$

with

$$E_n(t) = \beta^2 \hbar\omega_k - \hbar\Omega_\Delta(t) + n^2 \hbar\omega_k + n \left(2\beta \hbar\omega_k + \hbar\dot{\phi}(t) \right), \quad (10)$$

the two-photon recoil frequency

$$\omega_k = \frac{2\hbar k^2}{m}, \quad (11)$$

and

$$\beta = \frac{mv_0}{2\hbar k}. \quad (12)$$

The Schrödinger equation (9) is dimensionless in units of $\hbar\omega_k$; furthermore β is a dimensionless measure of the initial momentum relative to the rest frame. Thus, Eq. (9) is now independent of the particular choice of isotope mass m and the standing-wave wavenumber k . Since the common light shift $\Omega_\Delta(t)$ acts on all levels equally, it

only results in a global phase, and we may drop it. The structure of the “bare” ($\dot{\phi}(t) = 0$) momentum space states is shown in Fig. 1 (b) for $\beta = 0$. The energy levels form a quadratic ladder, coupled by the effective field $\Omega(t)$. In order for the excitation to be resonant for the various momentum-state transitions, $\dot{\phi}(t)$ has to be chosen to match the energy gap of the transition. In the simplest case of a continuous wave laser, $\phi(t) = \omega_L t$, we have

$$E_n^{\text{Rabi}} = \hbar n^2 \omega_k + \hbar n \omega_L \quad (13)$$

and we can bring two arbitrary neighboring levels n_0 and $n_0 + 1$ into resonance by choosing

$$\omega_L = -\omega_k(2n_0 + 1). \quad (14)$$

Driving the system with this frequency induces Rabi cycling of the population between the levels n_0 and $n_0 + 1$.

3. ANALYTIC CONTROL SCHEMES

3.1 Train of Rabi Pulses

The simplest and most widely used scheme for implementing a full interferometer is to use a train of Rabi pulses, as e.g. in Ref. 20. Starting from momentum state $|0\rangle$, a $\pi/2$ pulse with a frequency ω_L to match the 0-1-transition, $n_0 = 0$ in Eq. (14), drives the system into an equal superposition of $|0\rangle$ and $|1\rangle$. A subsequent series of π pulses transfers the population from $|1\rangle$ to $|N_{\text{max}}\rangle$. At this point, the atomic cloud continues to evolve in the superposition of $|0\rangle$ and $|N_{\text{max}}\rangle$ for the duration of its “time of flight” to travel up the tower, possibly picking up a relative phase due to the influence of a gravitational gradient. At the turning point, a second series of π pulses implements the “mirror”, transferring population from $|N_{\text{max}}\rangle$ to $|1\rangle$, swapping $|0\rangle$ and $|1\rangle$ and transferring population from $|1\rangle$ back to $|N_{\text{max}}\rangle$. After another free time evolution as the atomic cloud falls down the tower, a final series of Rabi pulses recombines the superposition; first transferring the population from $|N_{\text{max}}\rangle$ to $|1\rangle$ and then applying a final $\pi/2$ pulse.

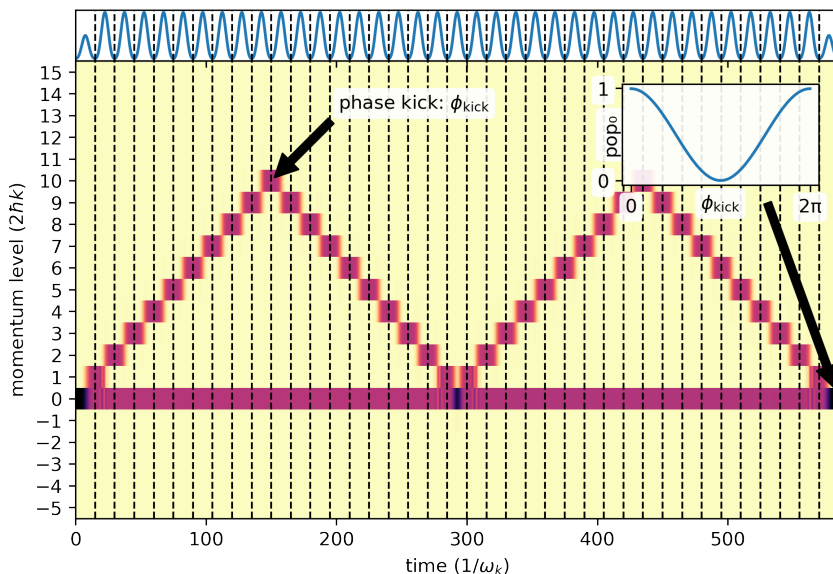


Figure 2. Momentum space dynamics under a train of Rabi pulses. The main panel shows the population in the momentum eigenstates for a system evolution starting from $|\Psi(t=0)\rangle = |0\rangle$. The state evolves under an initial and final $\pi/2$ pulse and a train of intermediate π pulses, with the pulse envelope shown in blue in the top panel. In the inset, the population in $|0\rangle$ at final time T as a function of an instantaneous phase kick ϕ_{kick} applied to $|N_{\text{max}}\rangle = |10\rangle$ as indicated by the first arrow.

The resulting ideal population dynamics in momentum space for $|N_{\text{max}}\rangle = |10\rangle$ is shown in Fig. 2. We have omitted the free time of flight which take place when the system is in the superposition of $|0\rangle$ and $|N_{\text{max}}\rangle$. As a

consequence, the final $\pi/2$ pulse returns the population entirely to the $|0\rangle$ state. In general, if we were to include a time of flight, the states $|0\rangle$ and $|N_{\max}\rangle$ would accumulate a relative phase. Numerically, we can emulate this phase by applying an instantaneous phase kick to the complex amplitude of only the level $|N_{\max}\rangle$, once the momentum state is fully split. Any such phase results in a superposition of $|0\rangle$ and $|1\rangle$ at final time T , where the population in $|0\rangle$ is

$$p_0 \equiv |\langle 0 | \Psi(T) \rangle|^2 = \cos^2\left(\frac{\phi_{\text{kick}}}{2}\right) = \frac{1}{2} + \frac{\cos(\phi_{\text{kick}})}{2}, \quad p_1 \equiv |\langle 1 | \Psi(T) \rangle|^2 = 1 - p_0. \quad (15)$$

This response to any accumulated relative phase is the core of the interferometer’s functionality as a sensing device.

In order to maximize signal contrast, Eq. (15) should be robust with respect to variations within the atomic cloud. Here, we focus on the two variations that most significantly limit signal contrast: first, variations in the effective pulse amplitude due to the transversal width standing wave, and second, variations in the initial velocity v_0 relative to the rest frame.

In order to evaluate robustness with respect to these parameters, we rewrite the Schrödinger equation. (9) as a system Hamiltonian

$$\hat{H} = \sum_n \left((E_n^{(0)}(t) + 2n\beta\hbar\omega_k) |n\rangle\langle n| - \mu S(t)(|n\rangle\langle n+1| + |n+1\rangle\langle n|) \right), \quad (16)$$

with

$$E_n^{(0)}(t) = n^2\hbar\omega_k + n\hbar\dot{\phi}(t). \quad (17)$$

This provides us with two dimensionless quantities (μ, β) that parametrize the robustness landscape. We define the “ideal” pulse amplitude as $\mu = 1$, in which case $S(t) = \Omega(t)$ in Eq. (9). Further, β as defined in Eq. (12) measures the initial velocity, with $\beta = 0$ for an atom that moves exactly at the rest frame velocity. We neglect the term proportional to β^2 in Eq. (9) under the assumption that $\beta \ll 1$. We have also neglected the common light shift $\Omega_\Delta(t)$, as it only contributes a global phase.

Figure 3 shows the result of propagating an initial state $|0\rangle$ under the Hamiltonian in Eq. (16) with a train of Rabi pulses as shown in Fig. 2. Each Rabi pulse targets a particular transition, cf. Eq. (14), with an amplitude calculated analytically to yield a pulse area of $\pi/2$ or π . The shown error is the deviation of the population in $|0\rangle$ at final time T from the ideal value of 1. Panel (a) maps the entire landscape, while panels (b) and (c) consider slices for fixed values of β and μ . The smallest error that we can reach is slightly above 10^{-4} for $(\mu, \beta) \approx (1.01, 0)$. The system is not particularly robust with respect to variations: deviating from the optimal values (μ, β) , the error quickly increases by several orders of magnitude. The presence of the surrounding levels fundamentally limits the fidelity of Rabi-cycling. That is, any given transition between a level n_0 and $n_0 + 1$ behaves only approximately as a two-level system that would allow to calculate the pulse area analytically. Indeed, the lowest error is not achieved for the “ideal” value of $\mu = 1$. We find that empirically, increasing the pulse amplitude by 1% over the amplitude predicted for a two-level system lowers the error by more than one order of magnitude.

As depicted in Fig. 3 (a, b), variations in μ result in a smooth increase of the error. This is expected, as an increase or decrease of pulse-amplitude simply overshoots or undershoots the Rabi pulse area, causing a cumulative population error on the same time scale as the overall pulse amplitude. In contrast, variations in β cause phase misalignments on a much faster time scale, resulting in the noisy response shown in Fig. 3 (a, c).

We note that the error in terms of the population $p_0(T)$ at final time T is a necessary but not a sufficient condition for the overall signal contrast of the interferometer. In addition, we would have to evaluate for each point (μ, β) whether the population in $|0\rangle$ and $|1\rangle$ reacts as expected to a phase kick being applied to the system, Eq. (15). We reserve such an analysis for future work.

3.2 Rapid Adiabatic Passage

As an alternative analytic pulse scheme to a train of Rabi pulses, rapid adiabatic passage (RAP) has been shown to be an effective method for momentum space transfer in an atomic interferometer.²¹ The well-established core

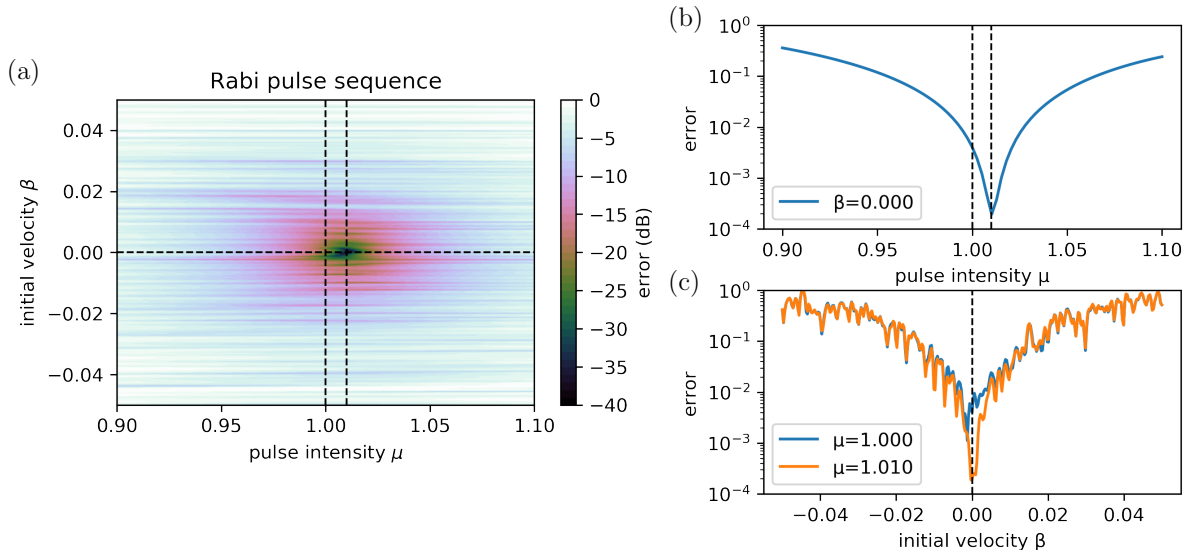


Figure 3. Robustness of the Rabi scheme depicted in Fig. 2. (a) Error of the population in $|0\rangle$ at final time T in decibel, i.e. $10 \log(1 - p_0(T))$, for a range of values μ around the ideal pulse intensity 1 and a range of values β around the ideal initial velocity 0. (b) Slice through the landscape for $\beta = 0$, corresponding to the horizontal dashed line in panel (a). The values $\mu = 1$ and $\mu = 1.01$ (best fidelity) are indicated. (c) Slice through the landscape for $\mu = 1$ and $\mu = 1.01$, corresponding to the two vertical dashed lines in panel (a).

concept of RAP is that chirping a laser pulse frequency adiabatically over a given transition induces population transfer. Remarkably, this transfer is independent of the pulse amplitude, as long as adiabaticity conditions are met. Thus, RAP has inherent robustness with respect to variations in pulse amplitude (μ) that we may be able to exploit towards a more robust atomic fountain interferometer.

More specifically, with respect to the momentum space Hamiltonian, Eqs. (9, 10) respectively Eqs. (16, 17), we choose the control phase

$$\phi(t) = -\frac{\alpha\omega_k(t - t_c)^2}{2} \quad (18)$$

to implement rapid adiabatic passage, with a linear chirp rate α and time offset t_c . This leads to time-dependent effective energy levels of

$$E_n^{\text{RAP}}(t) = n^2\hbar\omega_k - n\alpha(t - t_c)\hbar\omega_k. \quad (19)$$

Figure 4 shows how a single chirped pulse can be used to transfer momentum from $|0\rangle$ to e.g. $|10\rangle$. The top panel shows the smooth transfer of population, with crossings occurring at intervals of the Bloch time $\tau_B = 2/|\alpha|$. These correspond to crossings of consecutive energy levels $E_n^{\text{RAP}}(t)$ as defined in Eq. (19), shown in the second panel of Fig. 4 and marked by circles.

The offset time t_c accounts for the finite switch-on time of the pulse envelope (e.g. $t_{\text{rise}} = 25$), see the panel depicting $S(t)$ in Fig 4 and has to be determined empirically, $t_c = 7.8$ in this example. The small oscillations on top of the population curves are the result of a non-adiabaticity, due to the finite value of $\alpha = -0.1$, see the panel depicting $R(t)$.

Unfortunately, a full interferometer cannot be implemented with RAP pulses alone: The RAP mechanism allows for efficient population transfer, but it cannot realize the initial splitting of the wavefunction, or the SWAP gate implementing the interferometer’s “mirror”. This is despite the fact that RAP *can* produce a superposition of $|0\rangle$ and $|1\rangle$, starting from the initial state $|0\rangle$, by switching off the field at $t_c + \frac{\tau_B}{2}$ in Fig. 4. However, a subsequent RAP pulse to then transfer the population from $|1\rangle$ to $|10\rangle$ would also depopulate $|0\rangle$. Therefore, we must use Rabi pulses for the initial splitting, the SWAP gate, and the final recombination. We employ a

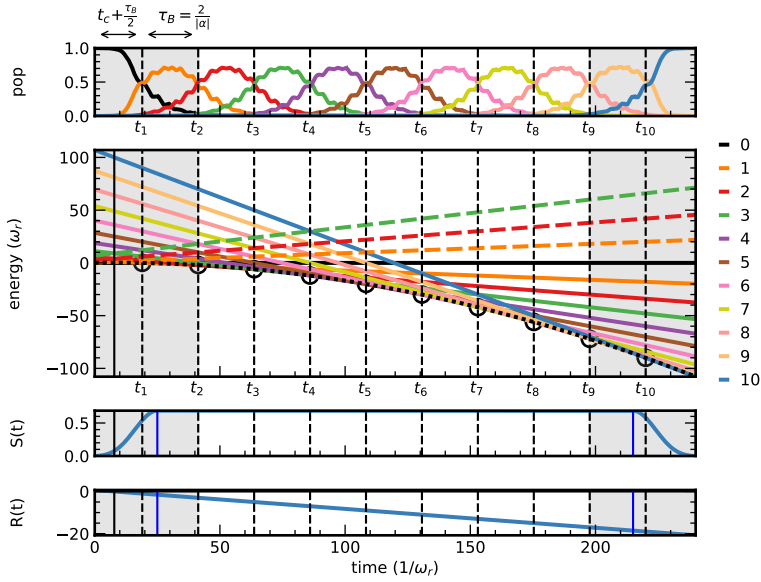


Figure 4. Momentum space transfer with rapid adiabatic passage (RAP). In the panels top to bottom, the population in levels $|0\rangle$ to $|10\rangle$, the time-dependent effective energy levels according to Eq. (19) for levels 0 to 10 (solid) and -1 to -10 (dashed), the pulse shape $S(t) = \Omega(t)$, and the linear chirp ramp, $R(t) = \frac{\alpha}{2}(t - t_c)$, cf. Eq. (18), with $\alpha = -0.1$.

$\pi/2$ pulse at the beginning and end of the interferometer, and add an additional π pulse to ensure that the wavefunction is sufficiently well-separated for the RAP scheme to be applicable. Likewise, we use a sequence of three π -pulses to implement the SWAP gate.

The resulting scheme for a full interferometer is shown in Fig. 5. Due to the adiabaticity requirement, the full scheme has a slightly longer duration than the comparable train of Rabi pulses in Fig. 2, as well as an increase in the pulse amplitude of the RAP pulses compared to the amplitude of the Rabi pulses. On the other hand, the scheme is conceptually much simpler. Also, at least in principle, RAP can be extended to reach arbitrary high momentum space excitation (beyond $|10\rangle$) as in the example of Figs. 4, 5), with a single control field for each transfer. The process is only limited by the experiment's ability to maintain a constant chirp rate.

In Fig. 6, we show the robustness of the RAP scheme, Fig. 5, in terms of the population in level $|0\rangle$ at final time T for different values (μ, β) (pulse amplitude and initial velocity). This compares directly to Fig 3 showing the robustness of the full Rabi scheme. We have adjusted the amplitude of the initial/center/final Rabi pulses employed in the RAP, by a factor of 1.01, corresponding to the empirical optimal value we were able to determine from Fig. 6 (a, b). Hence, the robustness landscape for the RAP scheme is centered at $(\mu = 1, \beta = 0)$. We are then able to observe the increase in robustness due to the use of rapid adiabatic passage for the population transfer: the scheme is robust over a much larger region, including an “echo” for variation in μ resulting from the interplay of the inherent independence of RAP of the pulse amplitude and the characteristics of the remaining seven Rabi pulses in the scheme. Slices through the parameter landscape in panels (b) and (c) of Fig. 6 show that we average an order of magnitude improvement in fidelity.

4. OPTIMAL CONTROL CONDITIONS FOR ROBUST ATOM INTERFEROMETRY

In the remainder of the paper, we explore the use of optimal control theory to further enhance the robustness of the interferometer. Conceptually, we can split the entire interferometer into 7 phases:

1. **Split** the initial state $|0\rangle$ into a superposition of $|0\rangle$ and $|N_S\rangle$
2. **Amplify** the superposition of $|0\rangle$ and $|N_S\rangle$ into a superposition of $|0\rangle$ and $|N_{\max}\rangle$

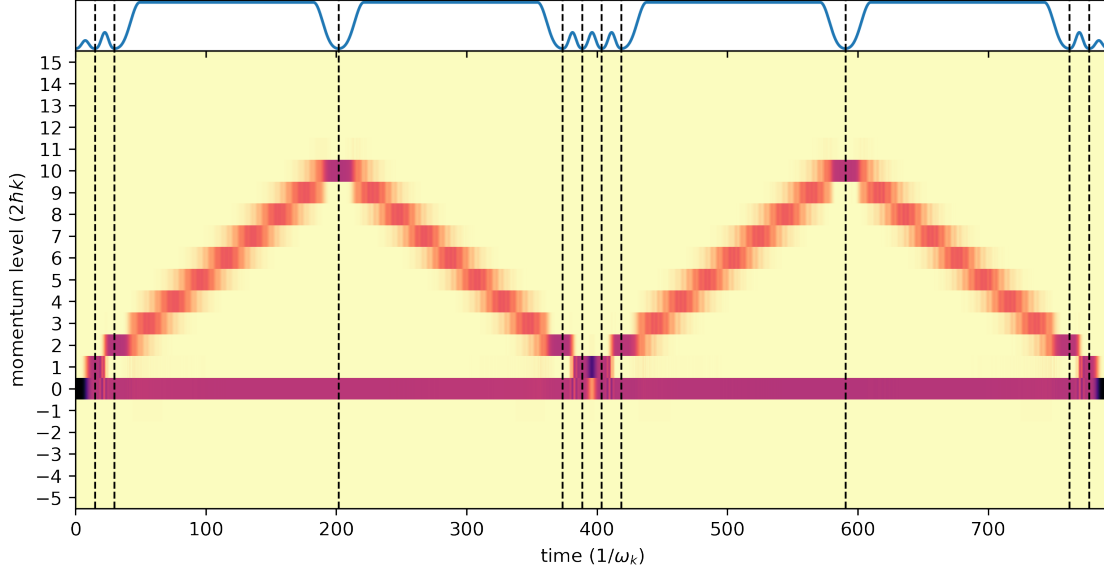


Figure 5. Momentum space dynamics under a scheme that uses rapid adiabatic passage (RAP) to obtain high-momentum states, cf. Fig 2.

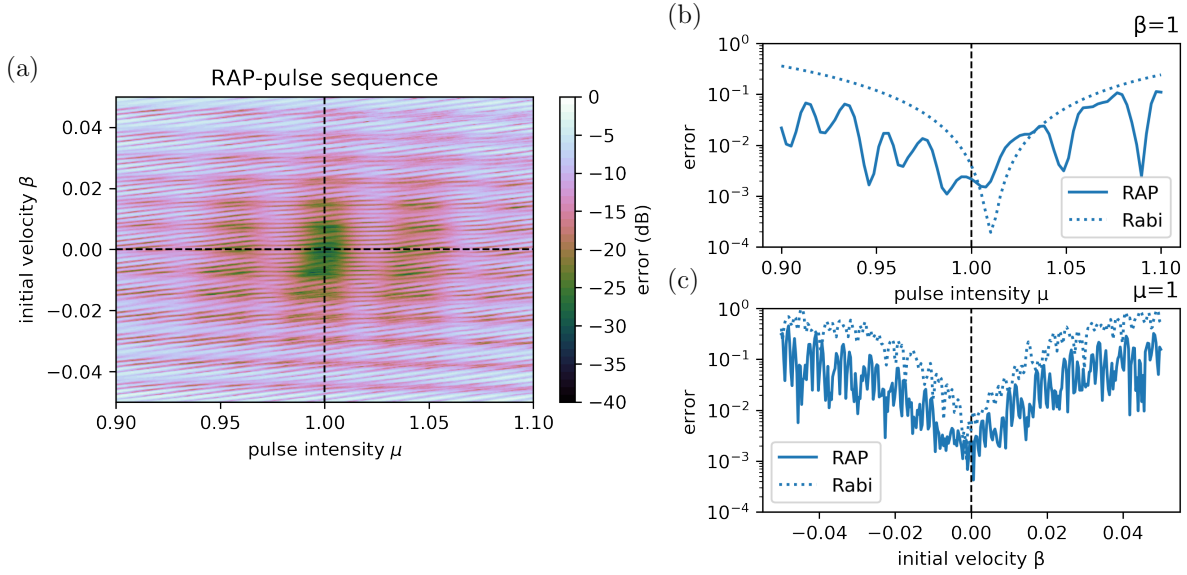


Figure 6. Robustness of the RAP scheme depicted in Fig. 5, cf. 3. In panels (b) and (c), the corresponding values from Fig 3 are indicated by the dotted line.

3. **De-amplify** the superposition of $|0\rangle$ and $|N_{\max}\rangle$ into a superposition of $|0\rangle$ and $|N_S\rangle$
4. **Swap** the states $|0\rangle$ and $|N_S\rangle$
5. **Amplify** as in step 2
6. **De-amplify** as in step 3
7. **Recombine** the superposition of $|0\rangle$ and $|N_S\rangle$ into $|0\rangle$, or a superposition of $|0\rangle$ and $|1\rangle$ as a function of the accumulated relative phase between $|0\rangle$ and $|N_S\rangle$.

We omit from this scheme the free time evolution. Instead, we may emulate the accumulated relative by applying an instantaneous phase kick after step 2, cf. Fig. 2. The choice of N_S here is arbitrary. At minimum, we can set $N_S = 1$. On the other hand, we may choose $N_S > 1$ to provide a minimum momentum separation for step 2, as we did in the RAP scheme with the initial $\pi/2$ and π pulses, see Fig. 5.

In any case, we have two fundamental requirements for any scheme implementing the full interferometer: First, the momentum space *population* must follow the seven steps listed above, and second, the *phase* dynamics must be such that the response to a phase kick is described by Eq. (15). This leads to a control condition for each of the above seven steps.

Consider the most general transformations that fulfill the population requirements for steps 1–6; for the initial splitter,

$$|0\rangle \rightarrow \frac{1}{\sqrt{2}} (|0\rangle + e^{\Delta\phi} |N_S\rangle) \quad (20)$$

with an arbitrary relative phase $\Delta\phi$; for the amplifier,

$$|0\rangle \rightarrow |0\rangle, \quad |N_S\rangle \rightarrow e^{i\phi_+} |N_{\max}\rangle, \quad (21)$$

with an arbitrary relative phase ϕ_+ ; for the de-amplifier,

$$|0\rangle \rightarrow |0\rangle, \quad |N_{\max}\rangle \rightarrow e^{i\phi_-} |N_S\rangle, \quad (22)$$

with an arbitrary relative phase ϕ_- ; and for the SWAP gate,

$$|0\rangle \leftrightarrow |N_S\rangle. \quad (23)$$

All of these are up to a global phase. For the final recombination, we have to take into account that it must map from $|0\rangle, |N_S\rangle$ to $|0\rangle, |1\rangle$, as the final time population must be entirely in the $|0\rangle$ - $|1\rangle$ subspace, as a function of the kick phase ϕ_{kick} according to Eq. (15). Thus we make the most general ansatz,

$$|0\rangle \rightarrow \frac{1}{\sqrt{2}} (e^{i\phi_{00}} |0\rangle + e^{i\phi_{10}} |1\rangle), \quad \text{and} \quad |N_S\rangle \rightarrow \frac{1}{\sqrt{2}} (e^{i\phi_{01}} |0\rangle + e^{i\phi_{11}} |1\rangle). \quad (24)$$

Evaluating steps 1–6 while applying $|N_S\rangle \rightarrow e^{i\phi_{\text{kick}}} |N_S\rangle$ after step 2, and then calculating the population in level $|0\rangle$ as $p_0 = |\langle 0 | \Psi(T) \rangle|^2$, we find

$$p_0 = \frac{e^{i\Delta\phi} e^{i\phi_{10}} e^{-i\phi_{11}} e^{i\phi_{\text{kick}}}}{4} + \frac{1}{2} + \frac{e^{-i\Delta\phi} e^{-i\phi_{10}} e^{i\phi_{11}} e^{-i\phi_{\text{kick}}}}{4}, \quad (25)$$

and similarly for the population in level $|1\rangle$,

$$p_1 = \frac{e^{i\Delta\phi} e^{i\phi_{10}} e^{-i\phi_{11}} e^{i\phi_{\text{kick}}}}{4} + \frac{1}{2} + \frac{e^{-i\Delta\phi} e^{-i\phi_{10}} e^{i\phi_{11}} e^{-i\phi_{\text{kick}}}}{4} \quad (26)$$

Remarkably, p_0 and p_1 do not depend on the phases ϕ_+ and ϕ_- . We can now determine the condition

$$\Delta\phi + \phi_{00} - \phi_{01} = 0, \quad \Delta\phi - \phi_{11} + \phi_{10} = \pm\pi \quad (27)$$

under which Eqs. (25, 26) become Eq. (15). Plugging this into Eq. (24), we find

$$|0\rangle \rightarrow \frac{e^{i\phi_{00}}}{\sqrt{2}} (|0\rangle + e^{i\Delta\phi} |1\rangle), \quad \text{and} \quad |N_S\rangle \rightarrow \frac{e^{i\phi_{10}}}{\sqrt{2}} (|0\rangle + e^{i(\Delta\phi+\pi)} |1\rangle) \quad (28)$$

with arbitrary phases ϕ_{00} and ϕ_{11} for the recombination. The entire analysis shows us that we can implement the interferometer without consideration of relative phases, except that a relative phase introduced by the initial splitter must be compensated by the final splitter. However, any relative phases introduced by amplification and de-amplification are irrelevant to the contrast of the interferometer. We have assumed that the SWAP gate is

exact up to a relative phase. In principle, we could also allow for the SWAP gate to introduce a relative phase. This phase would simply add to $\Delta\phi$ and would have to be compensated by the final recombination. To keep splitting and recombination symmetric, we avoid this approach as unnecessary and inelegant.

We may now further ask whether the initial splitter and the final recombination can be implemented with the same control field. Clearly, this is possible when using Rabi pulses: in Fig. 2, both components are realized with a $\pi/2$ pulse. As we need to fulfill Eq. (20) and Eq. (28) simultaneously, we must restrict the solution to $N_S = 1$. However, in this special case we find that Eq. (20) together with a unitarity condition $\hat{U}\hat{U}^\dagger = \mathbf{1}$ on the 0-1-subspace is equivalent to Eq. (28). This is a rather remarkable result: it implies that the only part of the interferometer that is in any way phase-dependent is the SWAP gate implementing the “mirror” halfway through the interferometer. All other control targets can be formulated by looking only at populations. This feature becomes especially interesting in the context of robustness with respect to deviations in (μ, β) , the effective pulse amplitude and initial velocity of the atoms: the relative phase in the two branches of the interferometer may depend on the value of (μ, β) without this affecting the expected interference response of the interferometer, Eq. (15).

5. ENSEMBLE OPTIMIZATION WITH KROTOV’S METHOD

Having derived the control conditions for the interferometer, we now formulate optimization functionals for a set of control fields that implement all parts of the interferometer (steps 1–7 listed in Section 4) and are robust with respect to variations in (μ, β) . First, we consider the initial splitter. As discussed in the previous section, the objective of the optimization is to split the initial state $|0\rangle$ into an equal superposition of $|0\rangle$ and $|N_S\rangle$, with an arbitrary relative phase. To this end, we define the target state

$$|\Psi\rangle^{\text{tgt}} = \frac{1}{\sqrt{2}} \left(|0\rangle + |N_S\rangle \right). \quad (29)$$

For a fixed value of (μ, β) , we can then define a functional

$$J_{\text{pop}}^{(0)} = \frac{1}{2} \sum_n \left(|\langle \Psi(T) | n \rangle|^2 - |\langle \Psi^{\text{tgt}} | n \rangle|^2 \right)^2, \quad (30)$$

where n runs over the momentum eigenstates, for the state $|\Psi(T)\rangle$ that is the result of propagating the initial state $|0\rangle$ under the Hamiltonian in Eq. (16) for some fixed duration T . The functional takes the minimum value of zero if and only if $|\Psi(T)\rangle$ has the same population in each level n as $|\Psi^{\text{tgt}}\rangle$, irrespective of the phase, see Appendix A for details.

If we choose $N_S = 1$ such that the control field implementing the initial splitting also implements the final recombination, we must ensure that the result is unitary in the 0-1-subspace. In this case, the unitarity condition is equivalent to $|1\rangle$ also mapping to a superposition of $|0\rangle$ and $|1\rangle$. We thus extend the functional in Eq. (30) to *simultaneously* optimize for a set of states $\{|\phi_k(T)\rangle\}$ where each state $|\phi_k(T)\rangle$ is the result of forward-propagating an initial state $|\phi_k\rangle$, and the populations in $|\phi_k(T)\rangle$ should match the population of a target state $|\phi_k^{\text{tgt}}\rangle$,

$$J_{\text{pop}}^{(K)} = \frac{1}{2} \sum_k \sum_n \left(|\langle \phi_k(T) | n \rangle|^2 - |\langle \phi_k^{\text{tgt}} | n \rangle|^2 \right)^2. \quad (31)$$

In our case, the sum over k runs over the values 0 and 1 and $|\phi_0^{\text{tgt}}\rangle = |\phi_1^{\text{tgt}}\rangle = |\Psi^{\text{tgt}}\rangle$ as defined in Eq. (29).

Lastly, we extend the functional once more to make the optimization robust with respect to the variations in the pulse amplitude, measured by μ , and the initial velocity, measured by β . To this end, we employ an *ensemble optimization*:¹⁷ for an ensemble of M pairs of values (μ, β) , we optimize for the average of the ensemble,

$$J_{\text{pop}} = \frac{1}{2M} \sum_{(\mu, \beta)} \sum_k \sum_n \left(\left| \langle \phi_k^{(\mu, \beta)}(T) | n \rangle \right|^2 - |\langle \phi_k^{\text{tgt}} | n \rangle|^2 \right)^2. \quad (32)$$

To minimize Eq. (32), we use Krotov’s method of optimal control^{9–15} to find a pulse shape $S(t)$ in Eq. (16), using a π -Rabi pulse as an initial guess. We allow $S(t) \in \mathbb{C}$. This is equivalent to allowing the laser frequency to vary.

Krotov’s method iteratively improves the control field by constructing an update^{15,16,22}

$$\Delta S^{(i)}(t) = \frac{S_0(t)}{\lambda_a} \text{Im} \left[\sum_{(\mu,\beta)} \sum_{k=1} \left\langle \chi_k^{(\mu,\beta),(i-1)}(t) \left| \left(\frac{\partial \hat{H}^{(\mu,\beta)}}{\partial S(t)} \right) \right|_{(i)} \phi_k^{(\mu,\beta),(i)}(t) \right\rangle \right], \quad (33)$$

for both the real and imaginary part of $S(t)$, where

$$\frac{\partial}{\partial t} \left| \phi_k^{(\mu,\beta),(i)}(t) \right\rangle = -\frac{i}{\hbar} \hat{H}^{(\mu,\beta),(i)} \left| \phi_k^{(\mu,\beta),(i)}(t) \right\rangle \quad (34)$$

in iteration (i) are the states propagated under the Hamiltonian $\hat{H}^{(\mu,\beta),(i)}$, that is, Eq. (16) for the particular values of μ and β and using the control field $S(t) = S^{(i)}(t)$. The “update shape” $S_0(t) \in [0, 1]$ is used to enforce the boundary conditions of $S(t) = 0$ at $t = 0$ and $t = T$, while λ_a is an inverse step width / “learning rate” that determines the overall magnitude of the pulse update. See Ref. 16 for details and how to choose these parameters. The co-states $|\chi_k^{(\mu,\beta),(i-1)}(t)\rangle$ are propagated backwards in time under the guess controls of iteration (i) , i.e., the optimized controls from the previous iteration $(i-1)$, as

$$\frac{\partial}{\partial t} \left| \chi_k^{(\mu,\beta),(i-1)}(t) \right\rangle = -\frac{i}{\hbar} \hat{H}^\dagger^{(\mu,\beta),(i-1)} \left| \chi_k^{(\mu,\beta),(i-1)}(t) \right\rangle, \quad (35)$$

with the boundary condition

$$\left| \chi_k^{(\mu,\beta),(i-1)}(T) \right\rangle = - \frac{\partial J_T}{\partial \left\langle \phi_k^{(\mu,\beta)}(T) \right\rangle \Big|_{(i-1)}}. \quad (36)$$

In Appendix A, this condition is evaluated for the functional in Eq. (32). Krotov’s method guarantees monotonic convergence and is particularly well-suited to find control fields with minimal constraints.¹⁶ However, other optimization methods such as gradient ascent (GRAPE)⁸ could also be used. In principle, the functional in Eq. (32) is non-convex and requires a second-order contribution to the pulse update.¹⁵ However, we find empirically that we can achieve monotonic convergence even with the first order update, for a sufficiently small step width (large λ_a).

In order to guarantee robustness over significant parts of the parameter landscape, a large number of quasi-randomly selected points (μ, β) may be required, potentially pushing the limits of what is numerically feasible. To remedy this, we can employ a *rotating ensemble*: We choose a relatively small number of points (μ, β) and optimize over that ensemble for some reasonable number of iterations (≈ 1000), before choosing a new set of points (μ, β) . This continues until convergence is reached and the entire landscape has been sufficiently sampled.

The interferometer’s remaining steps, i.e., the amplifier, de-amplifier, and SWAP are optimized in a similar procedure. The amplifier and de-amplifier can be optimized with the same functional of Eq. (32), with a single initial state $\Psi(t=0) = \frac{1}{\sqrt{2}}(|0\rangle + |1\rangle)$ and a target state $\Psi^{\text{tgt}} = \frac{1}{\sqrt{2}}(|0\rangle + |N_{\text{max}}\rangle)$ with e.g. $N_{\text{max}} = 10$. If we choose $N_S > 1$ such that we can be sure that the control field implementing the amplifier does not affect $|0\rangle$, we could also use a much simpler state-to-state functional²²

$$J_{\text{ss}} = 1 - \frac{1}{MK} \sum_{(\mu,\beta)} \sum_{k=1}^K \left| \left\langle \phi_k^{\text{tgt}} \left| \phi_k^{(\mu,\beta)}(T) \right\rangle \right|^2 \quad (37)$$

for the transition $|N_S\rangle \leftrightarrow |N_{\text{max}}\rangle$. Lastly, for the SWAP gate, use a standard gate optimization functional,²² adapted to the ensemble optimization,¹⁷

$$J_{\text{sm}} = 1 - \left| \frac{1}{MK} \sum_{(\mu,\beta)} \sum_{k=1}^K \left\langle \phi_k^{\text{tgt}} \left| \phi_k^{(\mu,\beta)}(T) \right\rangle \right|^2. \quad (38)$$

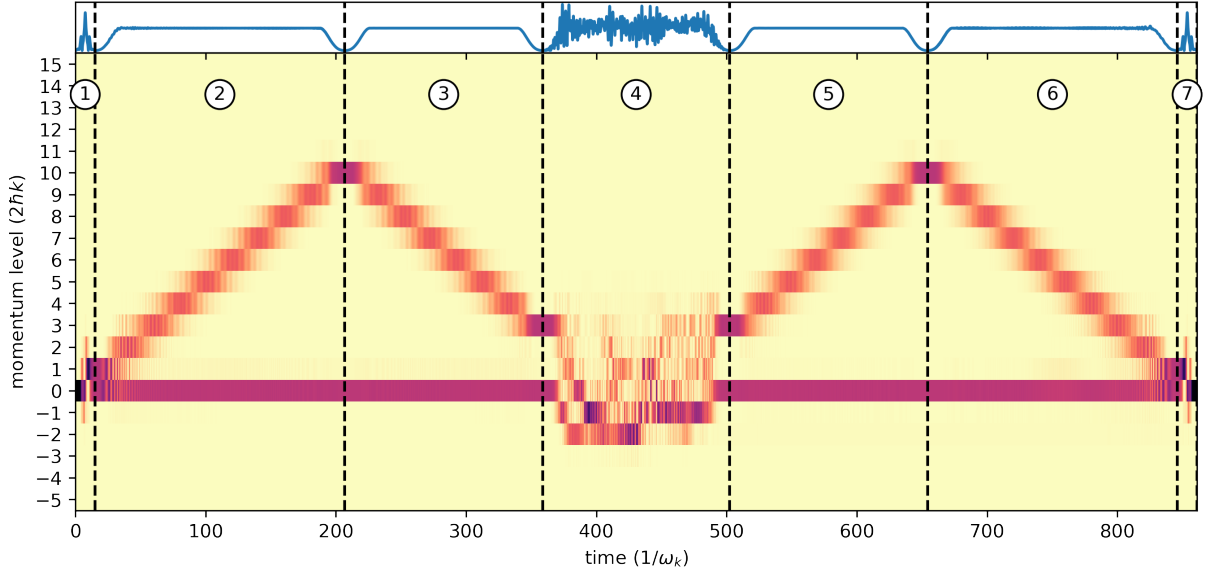


Figure 7. Momentum space dynamics under optimized pulses, cf. Figs. 2, 5. The control field for the time intervals marked (1) and (7) implements both splitting and recombination and is also shown in more detail in Fig. 9 (a-c) below. The control field implementing the SWAP between levels $|0\rangle$ and $|3\rangle$ in the interval marked as (4) is shown in Fig. 9 (d-f).

6. PRELIMINARY OPTIMIZATION RESULTS

Figure 7 shows some exemplary, albeit preliminary ensemble optimization results. The seven numbered sections correspond to steps 1–7 in Section 4. We have used $N_S = 1$ for the initial splitter in (1), allowing the same pulse to be used in (7) for the final recombination. However, for the SWAP gate in (4), we found the optimization task to yield a higher fidelity for $N_S = 3$ than for $N_S = 1$. The guess pulse for (1), (7) was a simple $\pi/2$ Rabi-pulse, as in Figs. 2, 5. The guess pulses for the different amplification/de-amplification steps, (2) with $N_S = 1$, (3) and (5) with $N_S = 3$, and (6) again with $N_S = 1$ used rapid adiabatic passage (RAP) as a guess pulse, using the same parameters as in Fig. 5. The optimization of these pulses for the ensemble is relatively straightforward; optimal control only introduces minor modulations on top of the guess which are barely visible in the shapes shown in Fig. 7. Lastly the SWAP gate in (4) used a RAP pulse with a V-shaped chirp profile as a guess pulse. We note that the chirp profile in any of guess pulses was considered static, although deviations from the prescribed chirp are possible due to $S(t) \in \mathbb{C}$.

The control field for (1) and (7) was obtained using a full rotating ensemble shown in Fig. 8 (a). Each batch consisted of 16 points, see the different color dots, for a total of 128 points. Within each batch, 1000 iterations were performed before cycling to the next batch. The remaining control fields, (2)–(6) only use a small fixed ensemble of 8 points shown in Fig. 8 (b) and are hence only preliminary. At these 8 points, Fig. 8 (c) shows the robustness of the entire scheme evaluated as a response to a phase kick after step (2). We can see that the interferometer is fully robust at these sample points.

Figure 9 shows the optimized control fields for the splitting/recombination, (1) and (7) as well as for the SWAP gate (4) in more detail. We note that the initial splitter has a simple robust solution. Even through optimization was allowed to select $S(t) \in \mathbb{C}$, the optimization converges to a solution with zero imaginary part, see panel (b). The optimization for the SWAP gate is considerably harder, and produces a much noisier pulse, see panel (d) as well as variations in the complex phase, see panel (f). The resulting spectrum in panel (f) pushes the limits of most current pulse shaping technology, especially in comparison to the simple spectrum in panel (c).

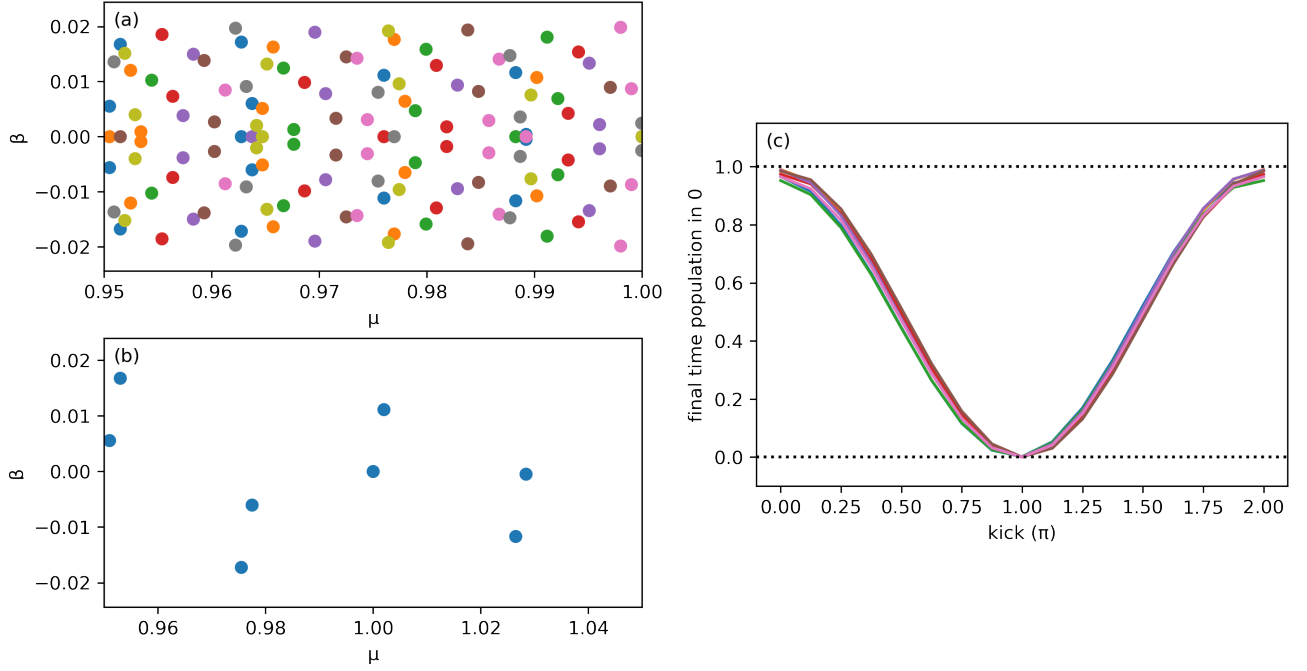


Figure 8. Ensemble points and contrast of the optimized scheme shown in Fig. 7. (a) Rotating ensemble used for the optimization of the pulse implementing splitting and recombination, in the intervals marked (1), (7) in Fig. 7. Each batch of 16 points is shown in a different color, combining to a total of 128 points. (b) Ensemble points used for the optimization of the control field in the intervals marked as (2-6) in Fig. 9. (c) Contrast curves for the eight values of (μ, β) in panel (b), showing the population in $|0\rangle$ at final time T as a functions of a phase kick applied to the maximum momentum state as shown in Fig. 2.

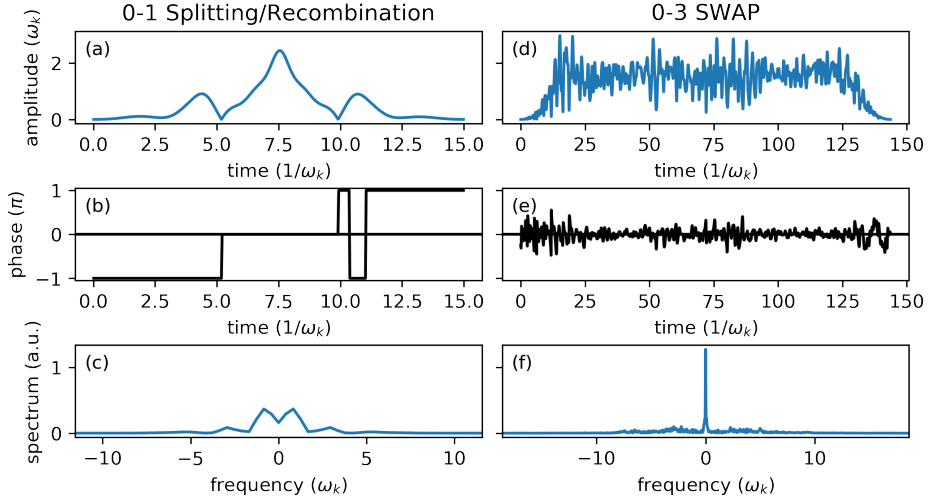


Figure 9. Example of optimized control fields. (a-c) The result of optimizing the transition of $|0\rangle$ into an equal superposition of $|0\rangle$ and $|1\rangle$, using the functional in Eq. (32) with a rotating ensemble of batch size 16 for a total of 128 points (μ, β) , see Fig 8 (a). (d-f) The result of optimizing for a SWAP in the two-level subspace $|0\rangle, |3\rangle$, using the functional in Eq. (38) and an ensemble of 8 points (μ, β) , see Fig 8 (b). Panels (a) and (d) show the absolute value of the pulse amplitude, panels (b) and (e) the complex phase in units of π , and panels (c) and (f) the spectrum in arbitrary units.

7. CONCLUSIONS AND OUTLOOK

We have derived a momentum space model for an atomic fountain interferometer in the Raman regime, for an atom interacting with two counter-propagating standing waves. In this model, we obtained a quadratic momentum ladder where individual transitions can be shifted into resonance by the derivative of the effective phase of the driving field. Population transfer is then driven by an effective two-photon transition. This allows for a wide variety of possible schemes, and we have analyzed two analytic schemes in detail: a train of Rabi pulses and the use of rapid adiabatic passage (RAP).

We have identified two parameters that limit the contrast of the interferometer for a cloud of atoms: the effective pulse amplitude relative to the “ideal” amplitude, measured by a dimensionless parameter μ , with $\mu = 1$ in the ideal case, and the initial velocity of the atoms relative to the rest frame, measured by a dimensionless parameter β , that is, the initial momentum in units of $\hbar k$, where k is the standing wave number. We have analyzed robustness with respect to these parameters both for the scheme of Rabi pulses and the scheme using RAP, finding a significant benefit to using RAP due to its inherent independence of a specific pulse amplitude.

In order to go beyond the limits of simple analytic pulse schemes, we have explored the use of optimal control theory to generate robust pulses. To this end, we have derived the most general control conditions for all components of the interferometer. Surprisingly, we find that the interferometer shows the expected interference fringes independently of any relative phase that non-ideal values of (μ, β) may induce. That is, the optimization can largely be steered looking only at population. We were thus able to formulate a novel optimization functional for population transfer.

To optimize for robustness, we adapted the functional to the method of ensemble optimization: averaging over an ensemble of values (μ, β) simultaneously. To limit the use of numerical resources while still covering the entire robustness landscape, we introduce a rotating ensemble, where the optimization switches to a new ensemble of points (μ, β) periodically.

Preliminary results show this approach to be feasible. For a small ensemble of points, we were able to show robust contrast for the full interferometer. In future work, we plan to extend these results to the full robustness landscape and produce a set of optimized control fields that outperform the best RAP-based analytical schemes, while remaining experimentally feasible.

APPENDIX A. OPTIMIZATION FUNCTIONAL FOR POPULATION CONTROL

We define a functional for the transfer of a state $|\Psi(0)\rangle \rightarrow |\Psi^{\text{tgt}}\rangle$ where we do not care about relative phases. That is, if we write

$$|\Psi^{\text{tgt}}\rangle = \sum_n a_n^{\text{tgt}} |n\rangle \quad (39)$$

in an orthonormal basis $\{|n\rangle\}$, then any wave function

$$|\Psi(T)\rangle = \sum_n a_n |n\rangle \quad (40)$$

that fulfills $\forall n : |a_n|^2 = |a_n^{\text{tgt}}|^2$ should minimize the functional. Using the population vectors \vec{p} and \vec{p}^{tgt} with components

$$p_n \equiv |a_n|^2 = \langle \Psi(T) | n \rangle \langle n | \Psi(T) \rangle, \quad (41)$$

$$p_n^{\text{tgt}} \equiv |a_n^{\text{tgt}}|^2 = \langle \Psi^{\text{tgt}} | n \rangle \langle n | \Psi^{\text{tgt}} \rangle, \quad (42)$$

an appropriate functional (to be minimized) is

$$\begin{aligned} J_{\text{pop}} &= \frac{1}{2} \|\vec{p} - \vec{p}^{\text{tgt}}\|^2 \\ &= \sum_n \frac{1}{2} (p_n - p_n^{\text{tgt}})^2 \\ &= \sum_n \frac{1}{2} \left(p_n^2 - 2p_n p_n^{\text{tgt}} + (p_n^{\text{tgt}})^2 \right). \end{aligned} \quad (43)$$

The factor 1/2 is solely to compensate the square when calculating gradients of the functional.

For an optimization with Krotov’s method, the boundary condition of the backward propagation is

$$\begin{aligned}
|\chi\rangle &= -\frac{\partial J_{\text{pop}}}{\partial \langle \Psi(T) |} \\
&= \sum_n \left(\frac{\partial}{\partial \langle \Psi(T) |} (p_n p_n^{\text{tgt}}) - \frac{\partial}{\partial \langle \Psi(T) |} \left(\frac{1}{2} p_n^2 \right) \right) \\
&= \sum_n p_n^{\text{tgt}} \frac{\partial p_n}{\partial \langle \Psi(T) |} - p_n \frac{\partial p_n}{\partial \langle \Psi(T) |} \\
&= \sum_n (p_n^{\text{tgt}} - p_n) \frac{\partial p_n}{\partial \langle \Psi(T) |} \\
&= \sum_n [(p_n^{\text{tgt}} - p_n) \langle n | \Psi(T) \rangle] |n\rangle \\
&= \sum_n (p_n^{\text{tgt}} - p_n) a_n |n\rangle .
\end{aligned} \tag{44}$$

ACKNOWLEDGMENTS

This work was funded in part by the U.S. Army Research Laboratory under Cooperative Agreement Number W911NF-16-2-0147.

REFERENCES

- [1] Berman, P. R., ed., [*Atom Interferometry*], Academic Press, San Diego, CA (1997).
- [2] Tannor, D. J., [*Introduction to Quantum Mechanics: A Time-Dependent Perspective*], University Science Books, Sausalito, California (2007).
- [3] Shore, B. W., [*Manipulating Quantum Structures Using Laser Pulses*], Cambridge University Press (2011).
- [4] Glaser, S. J., Boscain, U., Calarco, T., Koch, C. P., Klöckenberger, W., Kosloff, R., Kuprov, I., Luy, B., Schirmer, S., Schulte-Herbrüggen, T., Sugny, D., and Wilhelm, F. K., “Training schrödinger’s cat: quantum optimal control,” *Eur. Phys. J. D* **69**, 279 (2015).
- [5] Dowling, J. P. and Milburn, G. J., “Quantum technology: the second quantum revolution,” *Phil. Trans. R. Soc. A* **361**, 1655 (2003).
- [6] Degen, C. L., Reinhard, F., and Cappellaro, P., “Quantum sensing,” *Rev. Mod. Phys.* **89**, 035002 (2017).
- [7] Nielsen, M. and Chuang, I. L., [*Quantum Computation and Quantum Information*], Cambridge University Press (2000).
- [8] Khaneja, N., Reiss, T., Kehlet, C., Schulte-Herbrüggen, T., and Glaser, S. J., “Optimal control of coupled spin dynamics: design of NMR pulse sequences by gradient ascent algorithms,” *J. Magnet. Res.* **172**, 296 (2005).
- [9] Krotov, V. F. and Fel’dman, I. N., “An iterative method for solving optimal-control problems,” *Engng. Cybernetics* **21**, 123 (1983).
- [10] Krotov, V., [*Global Methods in Optimal Control Theory*], CRC Press (1995).
- [11] Tannor, D., Kazakov, V., and Orlov, V., “Control of photochemical branching: Novel procedures for finding optimal pulses and global upper bounds,” in [*Time-dependent quantum molecular dynamics*], Broeckhove, J. and Lathouwers, L., eds., 347–360, Plenum (1992).
- [12] Somló, J., Kazakov, V. A., and Tannor, D. J., “Controlled dissociation of I2 via optical transitions between the X and B electronic states,” *Chem. Phys.* **172**, 85 (1993).
- [13] Bartana, A., Kosloff, R., and Tannor, D. J., “Laser cooling of internal degrees of freedom. II,” *J. Chem. Phys.* **106**, 1435 (1997).
- [14] Sklarz, S. E. and Tannor, D. J., “Loading a Bose-Einstein condensate onto an optical lattice: An application of optimal control theory to the nonlinear Schrödinger equation,” *Phys. Rev. A* **66**, 053619 (2002).

- [15] Reich, D. M., Ndong, M., and Koch, C. P., “Monotonically convergent optimization in quantum control using Krotov’s method,” *J. Chem. Phys.* **136**, 104103 (2012).
- [16] Goerz, M. H., Basilewitsch, D., Gago-Encinas, F., Krauss, M. G., Horn, K. P., Reich, D. M., and Koch, C. P., “Krotov: A Python implementation of Krotov’s method for quantum optimal control,” *SciPost Phys.* **7**(6), 080 (2019).
- [17] Goerz, M. H., Halperin, E. J., Aytac, J. M., Koch, C. P., and Whaley, K. B., “Robustness of high-fidelity Rydberg gates with single-site addressability,” *Phys. Rev. A* **90**, 032329 (2014).
- [18] Chiow, S.-w., Kovachy, T., Chien, H.-C., and Kasevich, M. A., “ $102 \hbar k$ large area atom interferometers,” *Phys. Rev. Lett.* **107**, 130403 (2011).
- [19] Steck, D. A., “Rubidium 87 D Line Data,” (2009).
- [20] Kovachy, T., Asenbaum, P., Overstreet, C., Donnelly, C. A., Dickerson, S. M., Sugarbaker, A., Hogan, J. M., and Kasevich, M. A., “Quantum superposition at the half-metre scale,” *Nature* **528**, 530 (2015).
- [21] Malinovsky, V. S. and Berman, P. R., “Momentum transfer using chirped standing-wave fields: Bragg scattering,” *Phys. Rev. A* **68**, 023610 (2003).
- [22] Palao, J. P. and Kosloff, R., “Optimal control theory for unitary transformations,” *Phys. Rev. A* **68**, 062308 (2003).